

Study on The Sensitive Properties of Hydrate Reservoirs Based on Seismic Stereoscopic Detection Technology

LIU Xueqin^{1, 2, 3}, XING Lei^{4, 5, 6}, QIN Zhiliang^{*1, 2, 3}, LIU Huaishan^{4, 5, 6}

1. Acoustic Science and Technology Laboratory, Harbin Engineering University, Harbin 150001, China;
2. Key Laboratory of Marine Information Acquisition and Security (Harbin Engineering University), Ministry of Industry and Information Technology; Harbin 150001, China ;
3. College of Underwater Acoustic Engineering, Harbin Engineering University, Harbin 150001, China
4. Key Lab of Submarine Geosciences and Prospecting Techniques, MOE and College of Marine Geosciences, Ocean University of China, Qingdao 266100, P.R China
5. Evaluation and Detection Technology Laboratory of Marine Mineral Resources, Qingdao 266100, P.R China
6. National Laboratory for Marine Science and Technology, Qingdao 266061, China

Abstract: Higher-precision determinations of hydrate reservoirs, hydrate saturation levels and storage estimations are important for guaranteeing the ability to continuously research, develop and utilize natural gas hydrate resources in China. With seismic stereoscopic detection technology, which fully combines the advantages of different seismic detection models, hydrate formation layers can be observed with multiangle, wide-azimuth, wide-band data with a high precision. This technique provides more reliable data for analyzing the distribution characteristics of gas hydrate reservoirs, establishing velocity models, and studying the hydrate-sensitive properties of petrophysical parameters; these data are of great significance for the exploration and development of natural gas hydrate resources. Based on a velocity model obtained from the analysis of horizontal streamer velocity data in the hydrate-bearing area of the Shenhu Sea, this paper uses three VCs (longitudinal spacing of 25 m) and four OBSs (transverse spacing of 200 m) to jointly detect seismic datasets consisting of wave points based on an inversion of travelt ime imaging sections. Accordingly, by comparing the differences between the seismic phases in the original data and the forward-modeled seismic phases, multiangle coverage constraint corrections are applied to the initial velocity model, and the initial model is further optimized, thereby improving the imaging quality of the streamer data. Petrophysical elastic parameters are the physical parameters that are most directly and closely related to rock formations and reservoir physical properties. Based on the optimized velocity model, the rock elastic hydrate-sensitive parameters of the hydrate reservoirs in the study area are inverted, and the sensitivities of the petrophysical parameters to natural gas hydrates are investigated. According to an analysis of the inversion results obtained from these sensitive parameters, $\lambda\rho$, V_p and $\lambda\mu$ are simultaneously controlled by the bulk modulus and shear modulus, while V_s and $\mu\rho$ are controlled only by the shear

modulus, and the latter two parameters are less sensitive to hydrate-bearing layers. The bulk modulus is speculated to be more sensitive than the shear modulus to hydrates. In other words, estimating the specific gravity of the shear modulus among the combined parameters can affect the results from the combined elastic parameters regarding hydrate reservoirs.

Key words: natural gas hydrate; stereoscopic detection; elastic modulus; sensitive parameters;

E-mail: 11226535203@qq.com

1 Introduction

The stereoscopic detection of areas in which natural gas hydrates occur involves the application of seismic detection techniques by various observation methods, such as marine horizontal streamers, vertical cables (VCs), ocean bottom seismometers (OBSs) and ocean-bottom cables (OBCs) (Fig. 1). To date, however, seismic exploration endeavors at home and abroad rarely use these techniques individually; instead, most seismic exploration is conducted with joint detection methods involving OBSs and marine streamers or VCs and marine streamers. N. Satyavani established a longitudinal and transverse wave velocity model based on a two-dimensional wide-offset depth migration profile of the Krishna-Godawali (KG) basin and 25 four-component OBS data records, following which the hydrate saturation of the study area was estimated based on the velocity model (Satyavani et al., 2015). OBS data have been used in a multitude of study areas, such as the Andaman Basin (Satyavani et al., 2014) and Kerala Konkan Basin (Singh et al., 2012), to constrain two-dimensional models and establish high-precision velocity models. At the same time, OBS data have been applied to estimate the

This article has been accepted for publication and undergone full peer review but has not been through the copyediting, typesetting, pagination and proofreading process, which may lead to differences between this version and the [Version of Record](#). Please cite this article as [doi: 10.1111/1755-6724.14305](https://doi.org/10.1111/1755-6724.14305).

This article is protected by copyright. All rights reserved.

magnitude of hydrate saturation in several other research areas, such as the Oregon Sea (Kumar et al., 2006), the North Cascadia margin (Dash et al., 2011), and the South China Sea (Qiu et al., 2011; Wang et al., 2014). Furthermore, several studies, for example, (Westbrook et al., 2008), The shear-wave velocity has been estimated based on OBS station data (Peacock et al., 2010; Exley et al., 2010). Quantitative research on gas hydrate was carried out in Hydrate Ridge, northern Canada, based on high-resolution, multifrequency and multicomponent OBS data, with which a multifrequency analysis of the effects of hydrate bottom-simulating reflectors (BSRs) was conducted (Petersen et al., 2007). Similarly, an OBS survey of the Central Norwegian Sea provided evidence of the presence of gas layers in the subsurface sediments (Mienert et al., 2005). An approach to determine whether a study area contains natural gas hydrate was developed based on differences between the longitudinal and transverse wave velocity curves (Xia et al., 2008). Subsequently, The design of a submarine seismic observation system was completed in 2011 and achieved good results based on a ray-based tracking method (Wu et al., 2011). Zhang Guangguang and others obtained imaging profiles of subsurface reflection interfaces with high-resolution, high-spectrum 3D seismic and OBS data and further reported both the relationship between the longitudinal and transverse wave velocities and the variation characteristics of a gas hydrate reservoir (Zhang et al., 2014). Sha Zhibin et al used OBS four-component data in 2015 to study the distributions of gas hydrate reservoirs and the reservoir velocity in the northern part of the South China Sea (Sha et al., 2015). The role of OBS data in ascertaining the evolution of regional tectonism and in imaging the crustal structure is studied (Li et al., 2018; Wan et al., 2016). Most recently, Zhao Weina et al presented a geological interpretation utilizing OBS multicomponent data and obtained detailed information on the subsurface (Xia et al., 2016; Zhao et al., 2017).

Western countries such as the United States and Mexico have previously used VCs to perform both theoretical and applied technological research. Based in Texas in the United States, TEXACO owns the patent on VC seismic detection technology; in addition, companies such as Shell and Petroleum Geo-Services (PGS) are also based in the West. Following its implementation in the Gulf of Mexico, VC seismic exploration technology has been widely used in actual production endeavors. The application of VCs is of great significance for regional seismic imaging and high-resolution seismic detection. In 2009, JGI Japan applied VC technology to the detection of sulfide mineral deposits and explored VC data

processing-related technologies. At the same time, a VC exploration integrated system was developed, and both two-dimensional and three-dimensional detection experiments were successfully carried out in Wuhu. In 2010, the successful development of an autonomous VC detection system with a detection depth of 100-2000 m further advanced the applicability of VC data processing technology. Then, a joint VC and submarine source was first applied in 2013 to conduct 3D seismic exploration within the Okinawa Trough to investigate vulcanization, thereby providing valuable seismic data for structural studies of mineral deposits (Asakawa et al., 2012; 2015). In contrast, the field of VC research in China is in its infancy. Ward was the first to translate and study the feasibility of a VC seismic acquisition system (Ward et al., 1998). The full waveform inversion method was employed to analyze the area over which a VC acquisition system can be deployed (Bian et al., 2015). Huang Jianyu and others conducted experimental research on the key technologies of natural gas hydrate VC seismic systems, thereby accumulating experience in VC instrument research and development, field construction methods, and data acquisition technologies (Huang et al., 2016). Most recently, the optimization design of a VC observation system was studied (An et al., 2018).

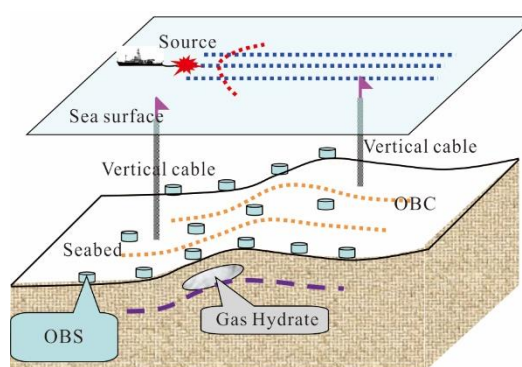


Fig. 1. Seismic stereo hydrate detection system

Marine seismic exploration is an important tool for the exploration of marine gas hydrate resources (Hao et al., 2017; Liao et al., 2016; Zhu et al., 2017; Zhang et al., 2016). However, with the continuous development of marine exploration technology and the ongoing growth and utilization of marine resources, the technical demands required for the exploration of marine resources is increasing, and higher-resolution, more advanced seismic exploration methods have become the focus of current research. Ocean stereoscopic detection is a new artificial seismic exploration method that integrates multidirectional observations from sources such as ocean streamers, OBSs, VCs and OBCs. Compared with a single conventional seismic

exploration technology, an ocean stereoscopic detection system can obtain data along different orientations, from different wavefields and in different frequency bands. Therefore, based on the characteristics of wide-angle, wide-band and stereoscopic three-dimensional seismic observation data from the Shenhu Sea area, this paper establishes a high-precision data model, images the subsurface formations, and inverts for the corresponding sensitive attributes.

2 Geological overview

The Shenhu Sea area is located on the northern continental slope of the South China Sea along the tectonic edge of the East Asian continent in a region characterized by the convergence of three tectonic plates (Fig. 1) (Wu et al., 2018; Ye et al., 2018). The special geological environment of the study area provides excellent conditions for the formation of natural gas hydrates and other resources (Yu et al., 2004). Research on the geology and resources of the region has always constituted a research hotspot for scientists, and thus, a plethora of studies have been published on the tectonic evolution of the study area. Accordingly, continuous geochemical, geophysical and geological research has confirmed that the temperature and pressure conditions and geological environment of the northern slope of

the South China Sea are conducive for the accumulation of natural gas hydrate (Naehr et al., 2000; Pierre et al., 1999; Trotsyuk et al., 1985; Waseda et al., 1998).

Previous studies analyzed the sedimentological evolution of the study region from various perspectives involving regional lateral and vertical features in addition to local features. With regard to the lateral evolution of the region, the centers of subsidence are located in central depressions, such as the Pearl River Mouth Basin. Among these basins in the Shenhu Sea area, the sedimentation rate in the southwestern basin is the largest; this is especially true for the Quaternary, during which the sedimentation rate reaches 190 m/Ma. Regarding the vertical sedimentological evolution, the sedimentation rate from the Late Miocene to the Pliocene was relatively stable with a decreasing trend; by the Quaternary, the average settlement speed of the strata in this area showed a sharp increase. Finally, based on an analysis of the subsidence rates of local formations, the formation settlement rates of the basin boundary areas and fold and fault zones change rapidly. Hence, the sedimentary and tectonic backgrounds during this period provide favorable geological conditions for the development and accumulation of natural gas hydrate resources in this area (Cong et al., 2013; Su et al., 2014).

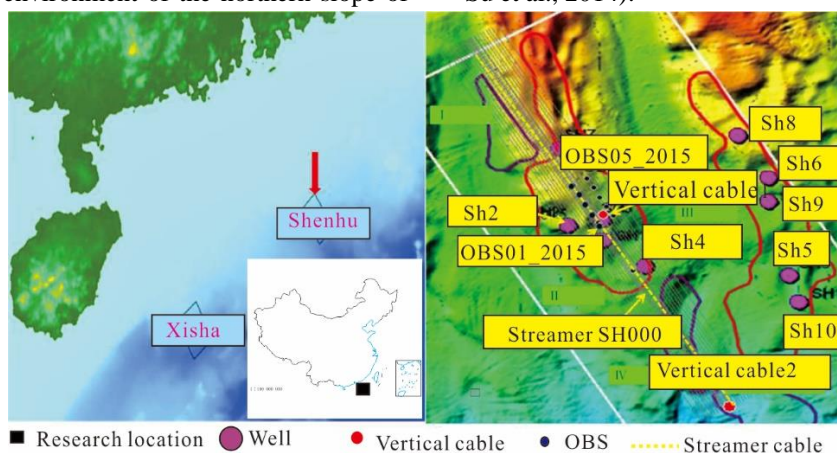


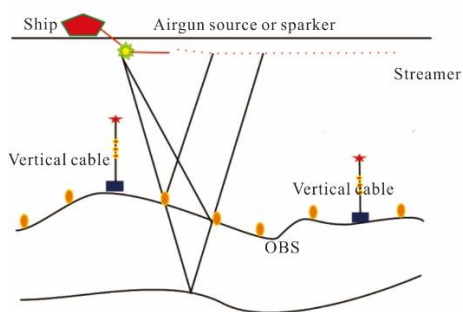
Fig. 2 Working area in the Shenhu Sea region

Since the Paleogene (23.8 Ma), the Enping Formation and Wenchang Formation located at depth beneath the study area have exhibited a large number of hydrocarbon generation stages. During the Dongsha movement, the fault structures in these formations from deeper to shallower depths were all active, and large amounts of pyrite dissolved in fluid matter were transported upwards from deeper strata through active faults (regional large-scale faults) and diapir structures. As the pressure gradually reduces, hydrocarbon gases gradually precipitate from these fluids. When free gas migrates into the Pliocene and Quaternary, it becomes

connected to deepwater fan faults and slip faults and continues to spread horizontally along low-angle faults. Since the Quaternary sedimentary layer is relatively dense and some of the abovementioned faults act as traps, upward-migrating free gas will continuously accumulate beneath the fault; then, when the free gas content reaches the saturation threshold of the hydrate formation, the hydrate will precipitate, thereby completing the formation and aggregation of the natural gas hydrate deposit (Wu et al., 2018; Ye et al., 2018).

On June 7-14, 2015, a stereoscopic detection sea trial (equipped with single-source, single-cable marine horizontal streamers, OBSs

and VCs) was carried out in the Shenhu Sea area with Struggle No. 4 and the Treasure Ship. A total of 11 OBS stations and 2 VC sets were installed, and 24 lines of multichannel seismic surveys were completed over a total distance of 369.7 km. The layout of the work area is shown in Fig. 3. For the horizontal streamers, a unilateral receiving observation system was adopted with a single-sided cannon and 360 channels, and the fold number is 45. Fifteen OBSs were divided into three groups, each of which was set on the ocean bottom for the collection of data with a spacing of 500 m. The VCs were a homemade OBS anchor system composed of three OBSs in series, where each OBS is equivalent to one node on the VC, with a spacing of 25 m. A floating ball was hung above the OBSs, and a cement weight was placed underneath; these cement weights and floating



balls were used to ensure that the VC descended smoothly to the seafloor (Fig. 4).

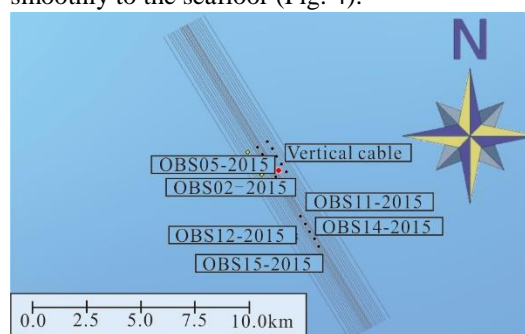


Fig. 3 Work area layout in the Shenhu Sea area black dots are OBS stations, yellow points are alternate OBS stations, red dots are VCs, and gray lines are the joint acquisition lines.

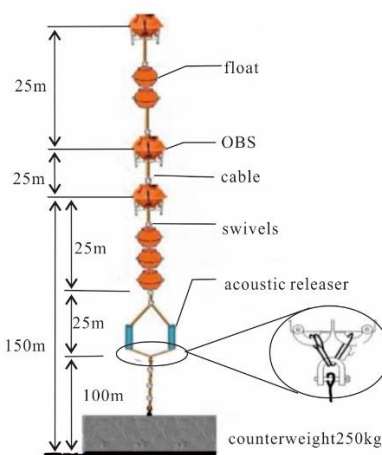


Fig. 4 Stereo detection system (left) and VC structure (right)

3 Model establishment and optimization based on stereoscopic detection data

3.1 Streamlining data to obtain the initial velocity model

According to the hyperbolic principle of seismic data, the seismic data are extracted into common midpoint (CMP) gathers (Fig. 5), and velocity analysis is performed to obtain the subsurface velocity profile (Fig. 6), after which seismic migration imaging is performed along line SH000 (Fig. 7).

3.2 Model optimization based on OBS data

Based on the initial velocity model obtained by streamer data, the OBS common detection point data subjected to secondary positioning and polarization filtering are used as constraints, and travelt ime imaging constraints are applied to the initial velocity model.

These corrections are applied according to the following principles: to determine the positions and shapes of reflective layers by using the information of reflected waves; to determine the velocities of reflective layers by using the

information of refracted waves; and to interpolate the interlayer velocities. The P-wave velocity inversion process using OBS data is as follows:

(1) The OBS data are preprocessed (including secondary positioning, denoising, polarization filtering, etc.);

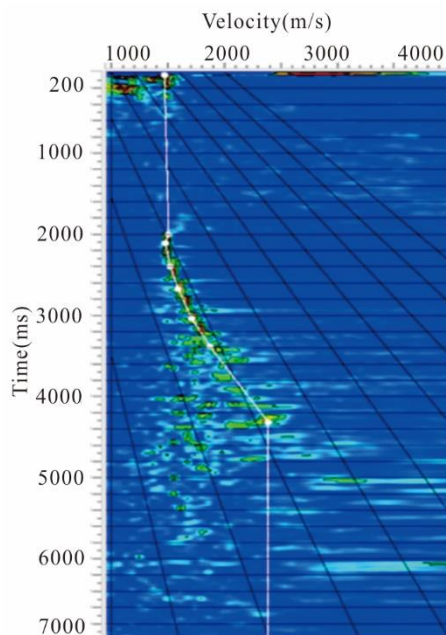


Fig. 5 Velocity analysis of a common midpoint (CMP) gather

(2) The P-wave velocity model obtained by streamer data is used as the initial model;

(3) Based on the initial model, the longitudinal wave velocities are inverted by recording longitudinal wave traveltimes in the OBS data, where the inversion proceeds from top to bottom, that is, after the first layer is determined, the second layer is inverted, and so on, until the final P-wave depth model is inverted.

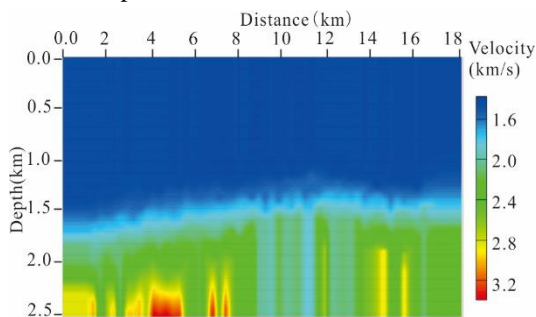


Fig. 6. Layered subsurface velocity field

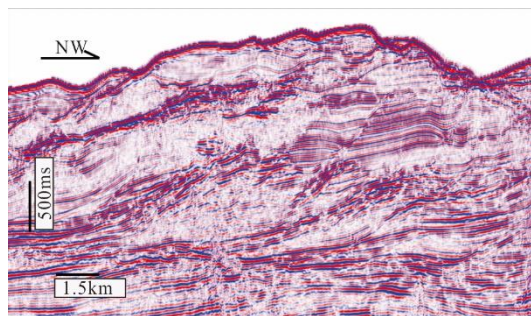


Fig. 7 Migration imaging section

Among the OBSs along line SH000, OBS01, OBS02, OBS03, and OBS05 boast a better data quality and clearer phases, with which reflected waves and refracted waves from multiple strata

can be identified (Fig. 8, Fig. 9, Fig. 10, and Fig. 11). OBS05 is taken as an example for seismic phase analysis (Fig. 12); this station is located at a distance of 9.4 km along the survey line, and five kinds of phases can be clearly identified on the section: red represents a direct wave, green and pink represent reflected waves from two formations, cyan denotes a seafloor refracted wave, and blue signifies a refracted wave from the hydrate reservoir. Local high-speed anomalies can be observed in the third layer of the constrained model (Fig. 13), representing the location of the hydrate reservoir (which is difficult to distinguish in the initial model). The P-wave velocity model corrections are applied based on the data from these four OBS stations arranged along parallel lines. The four OBSs are mutually corrected and mutually constrained, following which a parallel angle correction is applied to the model (Fig. 13).

3.3 Model optimization based on VC data

The P-wave velocity inversion using VC is performed as follows:

(1) The VC data are preprocessed (including geometric diffusion correction, denoising, filtering, etc.);

(2) The velocity model obtained after applying the OBS data constraint corrections is used as the initial model;

(3) Based on the initial model, the P-wave traveltimes in the VC data are picked, and then the P-wave velocity inversion is performed, where the inversion proceeds from top to bottom, that is, after the first layer is determined, the second layer is inverted, and so on, until the final P-wave depth model is inverted.

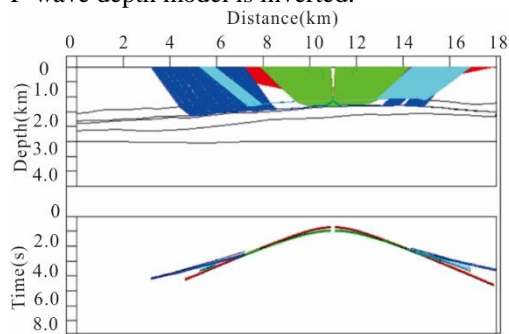


Fig. 8. OBS01 raypaths, traveltime imaging, and picked seismic phases

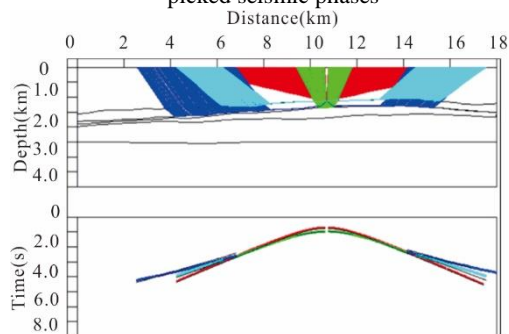


Fig. 9. OBS02 raypaths, traveltime imaging, and

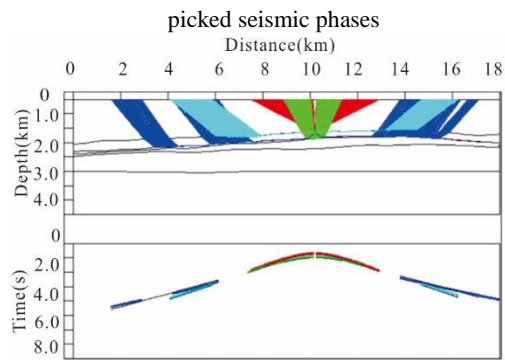


Fig. 10. OBS03 raypaths, traveltime imaging, and picked seismic phases

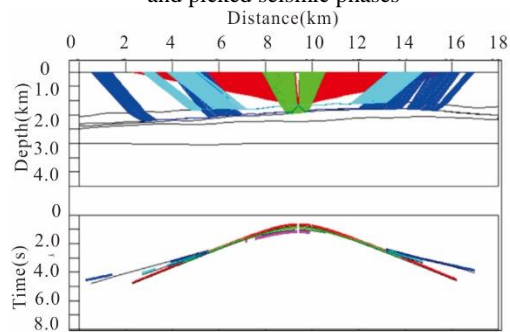


Fig. 11. OBS05 raypaths, traveltime imaging, and picked seismic phases

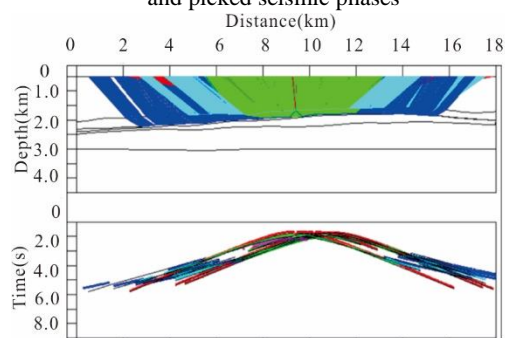


Fig. 12. Raypaths, imaged traveltimes and picked seismic phases from all four OBSs combined

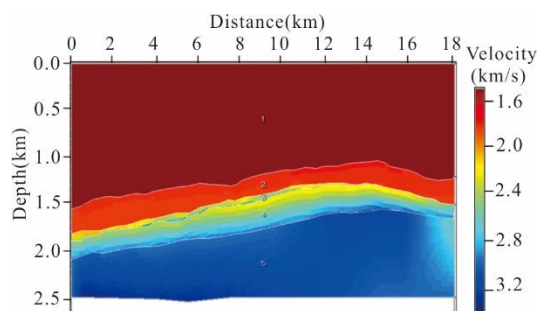


Fig. 13. OBS ray-based traveltime imaging correction velocity model

Three VC nodes, namely, VC01, VC02, and VC03, all of which are perpendicular to the profile, boast a better data quality and clearer phases, with which reflected waves and refracted waves from multiple strata can be better recognized (Fig. 14, Fig. 15, Fig. 16, and Fig. 17). VC01 is taken as an example to perform seismic phase analysis (Fig. 14); this node is

located at a distance of 11.2 km along the survey line, and five kinds of phases can be clearly identified in the section: red represents a direct wave, green and pink represent reflected waves from two formations, cyan denotes a seafloor refracted wave, and blue signifies a refracted wave from the hydrate reservoir.

Based on the corrections of the parallel angle applied to the velocity model of the OBS site data, the data from the three VC nodes are used to further apply vertical corrections to the OBS-modified model (Fig. 18). As shown in Fig. 13, the model bound by the OBS and VC data exhibits clearer, more defined boundaries for the hydrate reservoir (the high-speed anomaly in layer 3).

Fig. 24 Well logging correction results: the left plot shows the raw data, the middle panel displays the synthetic seismic record, and the right plot shows the correlation between the original record and the synthetic record (a high correlation with the hydrate occurrence area is denoted by yellow). Well SH2 logging results: the light blue curve on the left is the P-wave velocity (m/s), the middle green curve is the density (g/cc), and the gray curve on the right is the gamma curve.

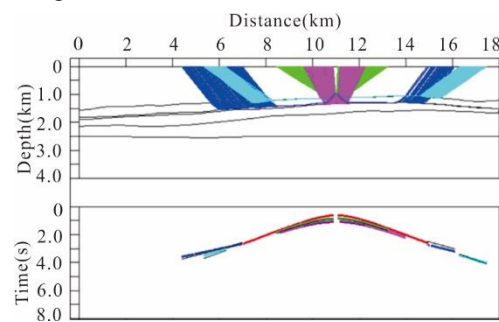


Fig. 14 Radiation traveltime imaging and seismic phase picking based on node VC01

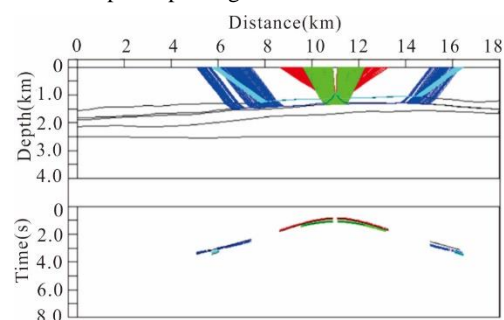


Fig. 15 Radiation traveltime imaging and seismic phase picking based on node VC02

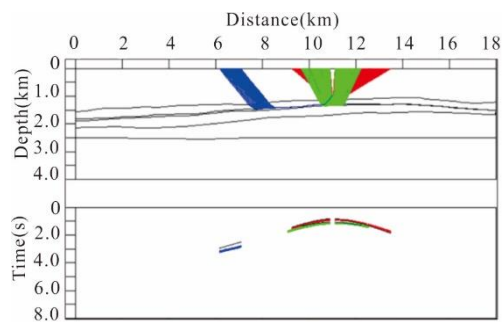


Fig. 16 Radiation traveltimes and seismic phase picking based on node VC03

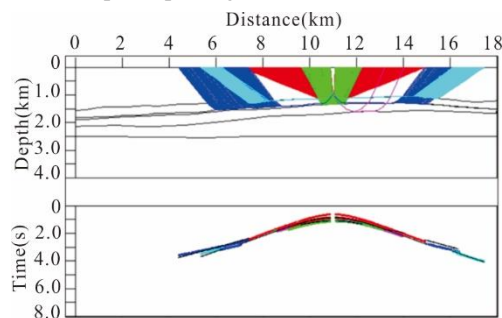


Fig. 17 Traveltimes and seismic phase picking based on the combination of the three VC nodes

According to the velocity model obtained by the joint constraint of OBS data and VC data (Fig. 18), the surface velocity of the seabed is about 1600 m/s (layer 2, quaternary) near the offset of 0 km. layer 3 is the stable layer of hydrate, and there is a significant velocity anomaly zone (offset 8-10 km, 4-6 km) with a sonic velocity range of 2200m/s-2600m/s. At the corresponding position

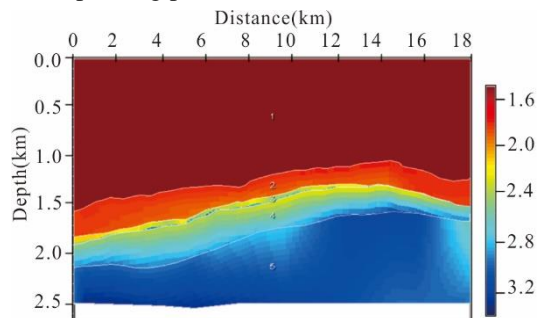


Fig. 18 VC+OBS model correction results

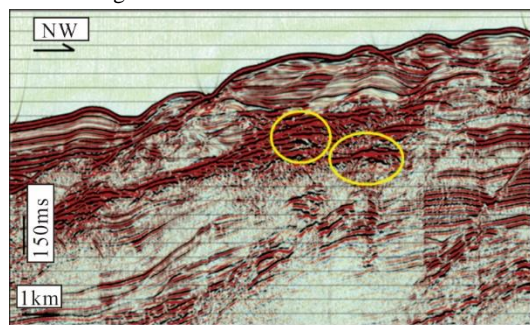


Fig. 19 Prestack depth migration profile before applying model constraints

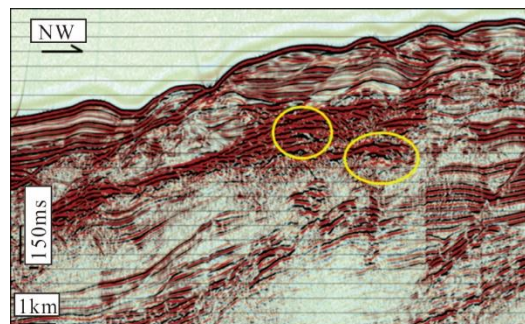


Fig. 20 Prestack depth migration profile based on OBS constraints

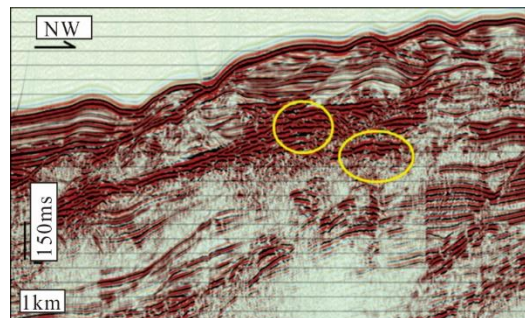


Fig. 21 Prestack depth migration profile based on both OBS and VC constraints

of the layer 4 below the velocity anomaly zone in the layer 3, there is a certain low velocity anomaly, which is likely to be a free gas zone. In addition, there is a wide range of low-speed anomaly areas in the layer 5 at an offset of 8-10 km. According to the geological structure analysis of the area, the low-speed anomaly area corresponds to the lower gas source migration channel, and the upward movement of a large amount of fluid medium causes a local decrease in formation velocity.

Fig. 19, Fig. 20, and Fig. 21 show the imaging results of the streamer data based on the superimposed velocity model and the constrained velocity model. Since the bottom of the hydrate layer in the OBS-corrected section is relatively flat, the velocity field obtained by the streamer data is already very accurate. The constrained velocity field, which is significantly improved, does not significantly change the imaging quality of the streamer data. According to the positions of the yellow circles in these figures, the bottom of the hydrate reservoir in the migration profile based on the OBS and VC constraints is clearer and more continuous, and it has a higher resolution. Therefore, based on three-dimensional seismic observation data from horizontal cables, VCs, and OBSs, a more accurate velocity model can be obtained to further improve the imaging quality of streamer data.

4 Assessment of the hydrate-sensitive parameters of hydrate reservoirs

4.1 Analysis of hydrate-sensitive parameter scatter plots based on well logging data

Fig. 22 displays a series of scatter plots pertaining to hydrate-sensitive parameters based on actual logging data acquired from the Shenhu Sea area. The horizontal axis of each plot is the hydrate saturation, while the vertical axes are the sensitive parameters, and the colored axis is the P-wave velocity, which is significantly correlated with the hydrate saturation (to determine the location of the hydrate in the intersection map) (Fig. 5). The region with a high P-wave velocity (shown in yellow) represents the hydrate target region in every plot (the red dotted line represents the linear relationship between the vertical and horizontal axes). In the scatter plots of the Poisson's ratio, S-wave velocity, and $\mu\rho$ versus the saturation, the hydrate reservoirs (regions with high P-wave velocities) are scattered, and there is no clear boundary between it and the surrounding rock. Although the relationships between these three variables and the hydrate saturation can be roughly defined, the regional distribution of gas hydrate will be difficult to determine using these

three parameters. In contrast, the boundaries between the hydrate reservoir and the surrounding rocks are clearer in the scatter plots of $\lambda\rho$ and $\lambda\mu$ versus the saturation. In the intersection plot between $\lambda\rho$ and the hydrate saturation, $\lambda\rho$ decreases as the saturation increases, and this change is consistent with changes in the surrounding rock. When the hydrate saturation is greater than 0.1 in the intersection plot between $\lambda\mu$ and the saturation, $\lambda\mu$ exhibits a linear relationship with the change in the saturation, but the slope of the line is small.

Evidently, in addition to the P-wave velocity, $\lambda\rho$ and $\lambda\mu$ both exhibit a good linear fit with the hydrate saturation, whereas other parameters, including Poisson's ratio, $\mu\rho$ and the S-wave velocity, exhibit relatively poor correlations with the hydrate saturation. When the hydrate saturation level is small, it is difficult to distinguish between the gas hydrate reservoir and the surrounding rock; moreover, as the hydrate saturation level increases, the sensitivities of these parameters decrease.

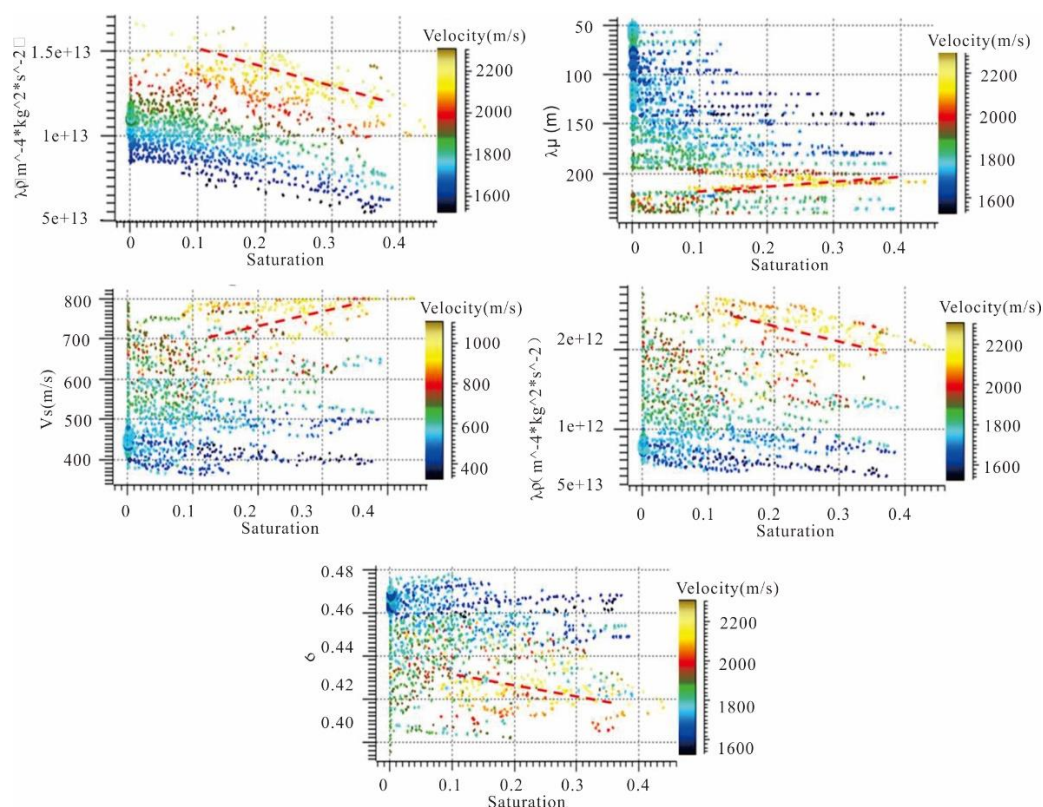


Fig. 22 Analysis of hydrate-sensitive parameters based on logging data from well SH2

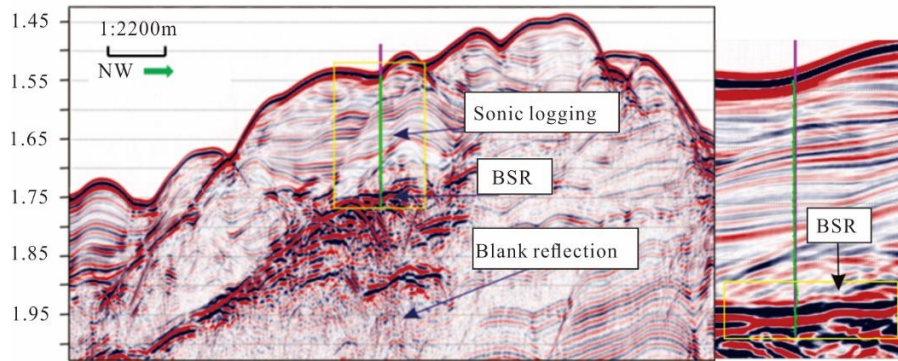


Fig. 23 Migration profile of line SH000 line (left) and partial magnification of the area around the well (right)

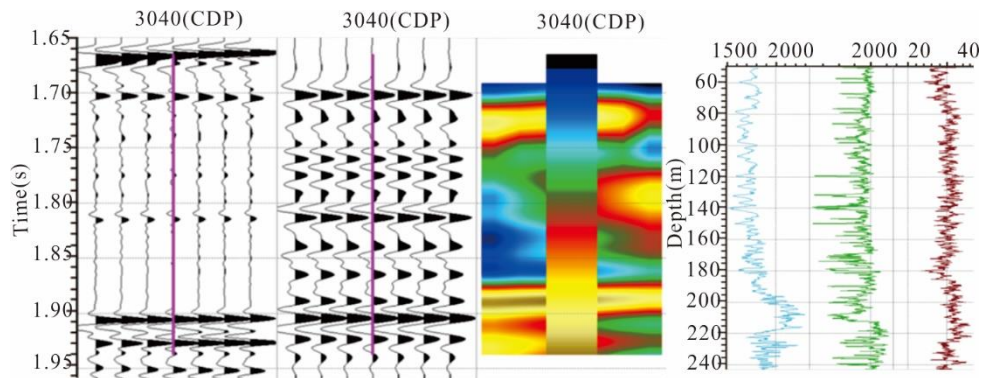


Fig. 24 Well logging correction results

the left plot shows the raw data, the middle panel displays the synthetic seismic record, and the right plot shows the correlation between the original record and the synthetic record (a high correlation with the hydrate occurrence area is denoted by yellow). Well SH2 logging results: the light blue curve on the left is the P-wave velocity (m/s), the middle green curve is the density (g/cc), and the gray curve on the right is the gamma curve

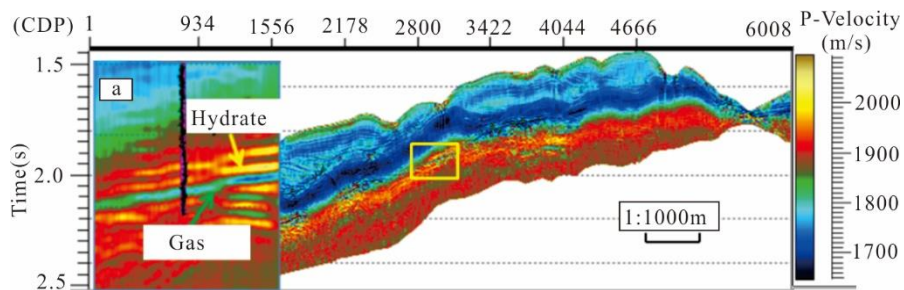


Fig. 25 Inversion profile of the P-wave velocity

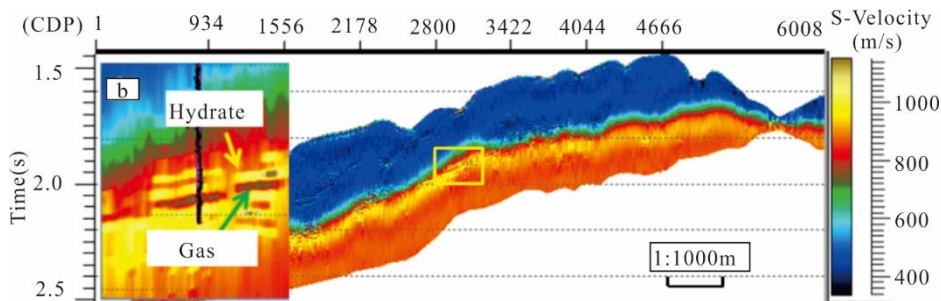


Fig. 26 Inversion profile of the S-wave velocity

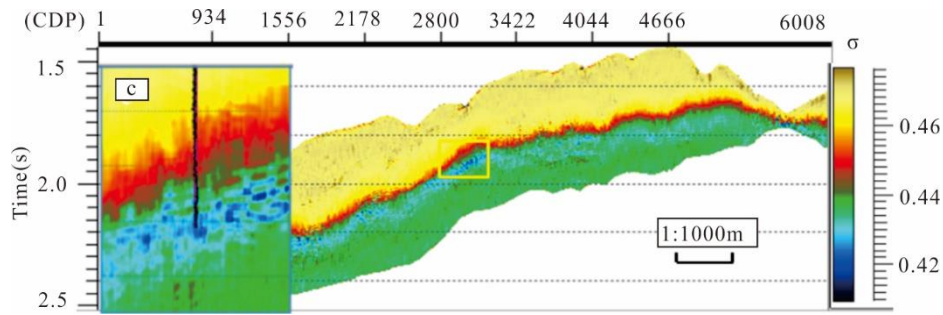
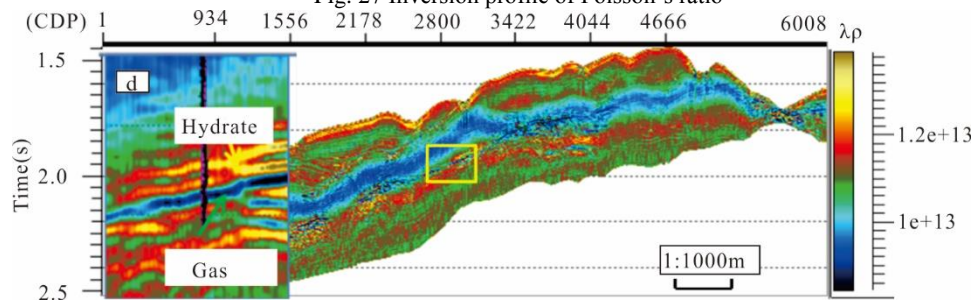
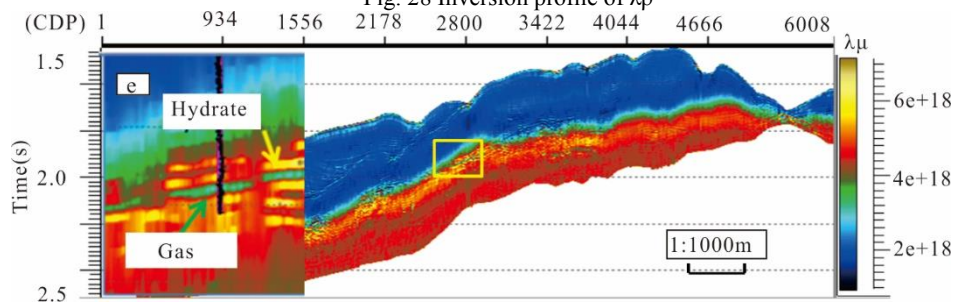
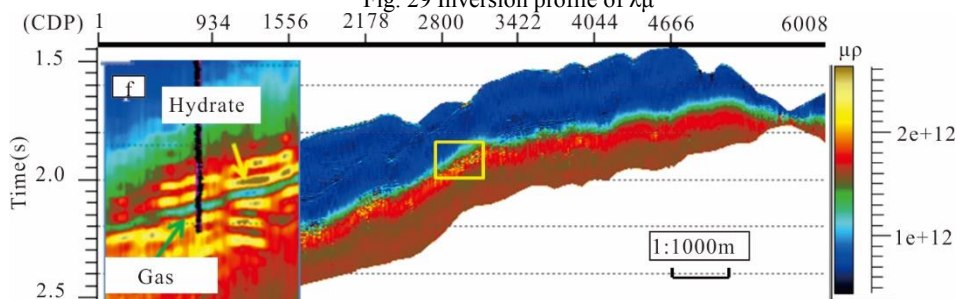


Fig. 27 Inversion profile of Poisson's ratio

Fig. 28 Inversion profile of $\lambda\rho$ Fig. 29 Inversion profile of $\lambda\mu$ Fig. 30 Inversion profile of $\mu\rho$

4.2 Inversion of hydrate reservoir-sensitive parameters in the Shenhu Sea area

Many kinds of attributes exist in the field of geophysical research. At present, the BSR effect, blank amplitude band, and amplitude versus offset (AVO) effect constitute the focus of natural gas hydrate research in China in addition to the estimation of hydrate saturation levels and the forward and inverse modeling of natural gas hydrates. However, with the rapid development of resource exploration technologies, the prestack seismic inversion method has become the core technology for predicting and describing hydrate reservoirs. Prestack seismic inversion is widely used to describe the physical characteristics of reservoirs and investigate their spatial distribution; furthermore, this method

provides a technical basis for reservoir trap predictions, past oil or gas storage determinations and sand body microstate descriptions. Therefore, to study the properties of natural gas hydrates and hydrate reservoir characteristics in more detail, this paper uses the prestack attribute parameter inversion method to extract multiple petrophysical parameters of natural gas hydrates and to study the sensitivities of these inverted petrophysical parameters to natural gas hydrates.

Table 1 provides the types and contents of sediments in the Shenhu hydrate reservoir. The composition of the solid rock consists of clay, sand and silt. In this paper, the physical parameters of sand and silt are assumed equivalent to those of quartz and calcite. The

fluid phase is mainly composed of water and gas components. A variety of gas components can be present within hydrates, including hydrocarbon gases (such as methane and ethane) and hydrocarbons (such as hydrogen, carbon dioxide and hydrogen sulfide). However, an air analysis of the sediments in the Shenhu area indicated that the main gas in the sediments of the Shenhu drilling area is hydrocarbon gas, with a maximum average methane content of 98% (Fu et al., 2010). Finally, the P-wave velocity and density of the logging data are taken as constraints. The clay content is 20% of the total solid content of the sediment, while 20% is calcite and 60% is quartz. Formation water accounts for 99% of the fluid phase, and the gas component accounts for 1%. In this case, the gas component is replaced by methane.

The seismic data used in this paper are derived from preprocessed two-dimensional horizontal streamer data along line SH000 (Fig. 3). According to the scale of the Shenhu Sea study area, three stacked datasets (with near, medium and far offsets) are extracted. Based on the logging data and seismic data from the study area (Fig. 23 and Fig. 24), multiple petrophysical parameters, such as the P-wave velocity, density and Poisson's ratio, are obtained by the prestack seismic inversion method. In this paper, a modified version of Shuey's approximation formula is employed; in the modified equation, the bulk modulus and shear modulus of the rock are used to replace the P-wave velocity and the S-wave velocity. The equations of the petrophysical parameters are expressed as follows:

$$R(\theta) \approx A + B\sin^2\theta + C(\tan^2\theta - \sin^2\theta) \quad (1)$$

$$A = \frac{1}{2} \left(\frac{\Delta V_p}{V_p} + \frac{\Delta \rho}{\rho} \right)$$

$$B = \frac{1}{2} \frac{\Delta V_p}{V_p} - 4 \frac{V_s^2 \Delta V_s}{V_p^2 V_s} - \frac{V_s^2 \Delta \rho}{V_p^2 \rho}$$

$$C = \frac{1}{2} \frac{\Delta V_p}{V_p}$$

$$\frac{\Delta V_p}{V_p} = 2 \left[\left(K_{sat_2} + \frac{4}{3} G_{sat_2} \right) \rho_1 + \left(K_{sat_1} + \frac{4}{3} G_{sat_1} \right) \rho_2 \right]$$

$$-4 \left[-2 \sqrt{\left(K_{sat_2} + \frac{4}{3} G_{sat_2} \right) \left(K_{sat_1} + \frac{4}{3} G_{sat_1} \right) \rho_2 \rho_1} \right] / \left(\left(K_{sat_2} + \frac{4}{3} G_{sat_2} \right) \rho_1 - \left(K_{sat_1} + \frac{4}{3} G_{sat_1} \right) \rho_2 \right)$$

$$\frac{\Delta V_s}{V_s} =$$

$$2 \left[G_{sat_2} \rho_1 + G_{sat_1} \rho_2 - 2 \sqrt{G_{sat_2} G_{sat_1} \rho_2 \rho_1} \right] / \left(G_{sat_2} \rho_1 - G_{sat_1} \rho_2 \right)$$

$$\frac{V_s^2}{V_p^2} = \frac{G_{sat}}{K_{sat} + \frac{4}{3} G_{sat}}$$

$$K_{sat_2} = K_{sat} + \Delta K_{sat}$$

$$K_{sat_1} = K_{sat} - \Delta K_{sat}$$

$$G_{sat_2} = G_{sat} + \Delta G_{sat}$$

$$G_{sat_1} = G_{sat} - \Delta G_{sat}$$

$$\rho_2 = \rho + \Delta \rho$$

$$\rho_1 = \rho - \Delta \rho$$

The elastic modulus of the rock skeleton in the study area can be obtained by using an equivalent medium model; as a result, the porosity is greater than the critical porosity. In this paper, the elastic modulus of a layer containing natural gas hydrate is studied by using the empirical formula of an equivalent medium model with a porosity greater than the critical porosity.

The relationships among the sensitive petrophysical parameters and the elastic modulus are expressed as follows:

$$V_p = \sqrt{\frac{K_{sat} + \frac{4}{3} G_{sat}}{\rho}} \quad (2)$$

$$V_s = \sqrt{\frac{G_{sat}}{\rho}} \quad (3)$$

$$\mu \rho = G_{sat} \rho \quad (4)$$

$$\lambda \rho = \left(K_{sat} - \frac{4}{3} G_{sat} \right) \rho \quad (5)$$

$$\lambda \mu = \left(K_{sat} - \frac{4}{3} G_{sat} \right) G_{sat} \quad (6)$$

$$\sigma = \frac{3K_{sat} - 2G_{sat}}{6K_{sat} + 2G_{sat}} \quad (7)$$

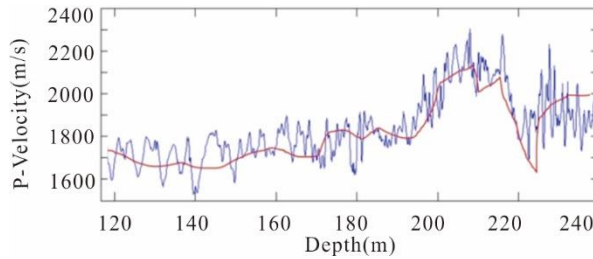


Fig. 31 Comparison of the P-wave velocity inversion results with well logging data the blue line represents the P-velocity logging curve, while the red line signifies the P-wave velocity inversion result

4.3 Sensitivity analysis of petrophysical parameters based on the inversion results

According to the rock elastic modulus obtained by the inversion, each sensitive parameter can be obtained by combining the

relationship between each sensitive parameter and the elastic modulus of the rock in Equation 1. The results of the inversion are in good agreement with the results of the well logging scatter plots. Notably, V_p , $\lambda \mu$, and $\lambda \rho$ clearly

reflect the hydrate distribution, and the hydrate reservoir location is in good agreement with the P-wave velocity trend. The P-wave velocity clearly reflects the spatial distribution of gas hydrate in the formation (Fig. 25, Fig. 28, and Fig. 29), and the P-wave velocity in the hydrate-bearing area reaches a maximum of 2200 m/s. An obvious low-velocity zone can be observed at the bottom of the reservoir where the P-wave velocity is significantly lower than that of the surrounding rock, reaching as low as 800 m/s. Previous studies have shown that significant sources of biogas and deep gas may exist in the Shenhu area (Herri et al., 1999; Kvenvolden et al., 1995); accordingly, the anomalous bands in the inversion results may be attributable to the presence of free gas (Fig. 26). The S-wave velocity exhibits a significant response to hydrate and free gas reservoirs, but high-velocity anomalies also occur below the suspected free gas reservoirs. The Poisson's ratio of the hydrate-bearing region is low, while that of the free gas area is even lower, which is consistent with the previous findings of Xiujuan (Fig. 27). As shown in Fig. 28, $\lambda\rho$ can reflect the hydrate distribution even more clearly than can the P-wave velocity (Fig. 28). Additionally, $\mu\rho$ can readily describe the locations of hydrates and suspected free gas; however, similar to the S-wave velocity, high-value anomalies exist below the suspected free gas reservoirs, where hydrate was not detected based on the P-wave velocity and well logs (Fig. 29). Finally, $\lambda\mu$, which is the product of the elastic and shear moduli, reflects the distribution of hydrates better than V_s ; moreover, $\mu\rho$ is associated only with the shear modulus and thus delineates the hydrate distribution less effectively than either V_p or $\lambda\rho$ (Fig. 30).

By analyzing the inversion results of the hydrate-sensitive parameters, the following conclusions can be drawn. $\lambda\rho$, $\lambda\mu$, and V_p are controlled by both the elastic modulus and the shear modulus, while V_s and $\mu\rho$ are controlled only by the shear modulus. Additionally, the latter two parameters are less sensitive to hydrate

saturation than are the former three. Therefore, as the number of relevant factors constraining a sensitive parameter increases, the sensitivity of that parameter to hydrates increases. In other words, the elastic modulus may be more sensitive to the presence of gas hydrate than is the shear modulus.

The inverted P-wave velocity results (Fig. 31) are in good agreement with the logging data, which suggests that the inversion results for the other sensitive parameters provide satisfactory references (Fig. 31). These findings provide guidance for the evaluation of hydrate reservoirs and the corresponding level of hydrate saturation.

4.4 Sensitivity analysis of petrophysical parameters based on saturation estimations

In this paper, the inversion results of various petrophysical parameters are used to estimate the saturation levels of hydrate reservoirs based on a neural network algorithm. The saturation inversion results obtained from the hydrate-sensitive parameters are consistent with those discussed above (Fig. 32). The results suggest that the saturation levels obtained from V_p , $\lambda\mu$ and $\lambda\rho$ are in good agreement with the logging saturation curves and boast a high resolution with a maximum saturation of 0.44; regardless of whether the hydrate saturation is high or low, the boundaries of the hydrate reservoir are clearly delineated. However, the saturation inversion results obtained from V_s and $\mu\rho$ differ from those of the logging curves with a maximum saturation of 0.43; these two parameters only vaguely indicate the hydrate boundaries, especially in areas where the hydrate saturation is low. The sensitivities of these two sets of parameters to hydrates are better than those in areas of high saturation (greater than 0.35), and the difference in the hydrate saturation level is small. When the saturation is low (less than 0.35), the sensitive parameters associated only with the shear modulus are less sensitive to hydrates. Although

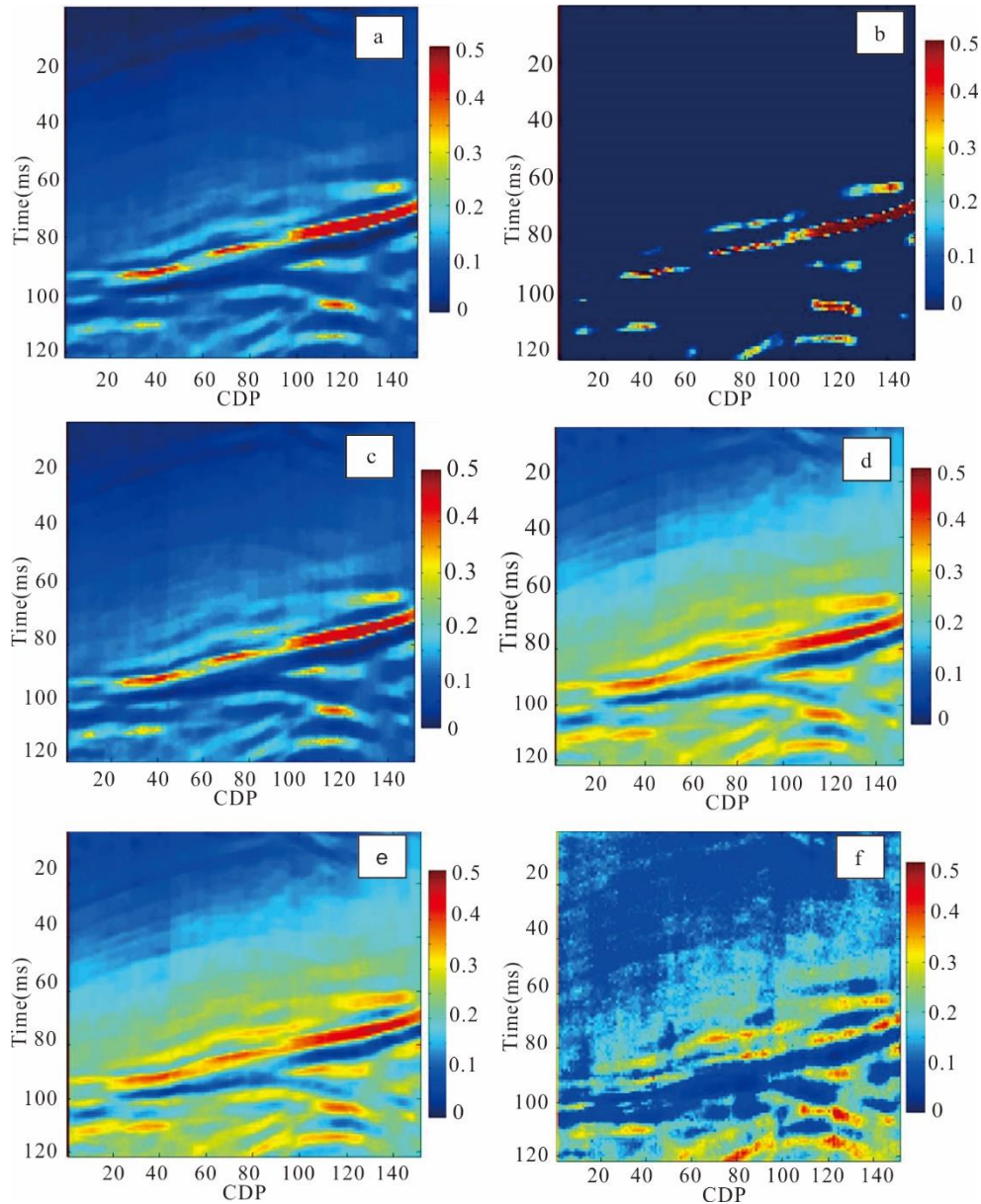


Fig. 32 Hydrate-sensitive parameter inversion results

a is the saturation inverted from V_p ; b is the saturation inverted from $\lambda\rho$; c is the saturation inverted from $\lambda\mu$; d is the saturation inverted from V_s ; e is the saturation inverted from $\mu\rho$; f is the saturation inverted from σ

Poisson's ratio is a function of both the shear modulus and the elastic modulus, the inversion result obtained from σ is the least ideal (but the free gas below the hydrate is well reflected). Notably, Poisson's ratio is more sensitive to hydrates, but this conclusion is applicable only when the hydrate is in a fluid phase within the rock pores. The presence of hydrate changes only the elastic modulus of the rock and does not affect the shear modulus of the rock skeleton or the S-wave velocity. In this case, Poisson's ratio

is highly sensitive to the hydrate saturation level. However, the gas hydrate present in the Shenhu Sea area is part of the rock skeleton, and its presence also affects both the elastic modulus and the shear modulus.

Thus, V_p and V_s will increase and decrease simultaneously, whereas Poisson's ratio is proportional to the ratio between these two values; therefore, Poisson's ratio cannot effectively describe the hydrate properties in the Shenhu Sea area.

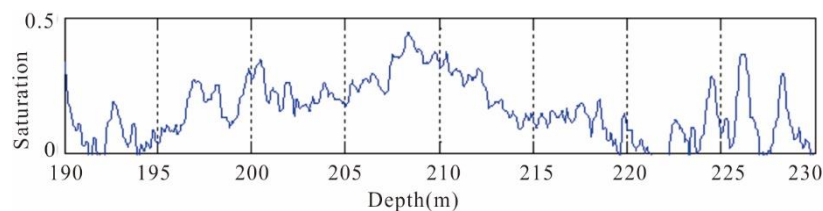


Fig. 33 Inversion results obtained from the hydrate-sensitive parameters

5 Discussion

The study of the properties of natural gas hydrate reservoirs based on the stereoscopic detection technique can provide some ideas and methods for the continued development and utilization of natural gas hydrates. At present, however, the application of stereoscopic detection for the detection of hydrate reservoirs at home and abroad has not been fully researched. Therefore, the author synthesizes the three-dimensional exploration results of hydrate reservoirs at home and abroad and proposes that the following work be performed in the future.

There is no precedent for recognizing and effectively suppressing noise within data obtained by a stereoscopic observation network, especially with regard to the suppression of multiples in integrated stereoscopic data. It is important to note that the most critical issue pertaining to all methods intended to suppress multiples is the identification and determination of multiples. Stereoscopic detection systems can help us identify multiples more accurately because a stereoscopic viewing grid can effectively determine and separate the wavelet directions. Thus, how to use information derived from the stereoscopic observation wavefield to identify and analyze multiples is a major problem that needs to be solved.

Constructing a complete and comprehensive processing method for stereoscopic detection data constitutes a key problem to be solved in future research. Ocean stereoscopic detection systems integrate different collection methods, such as horizontal cables, VCs and OBSs, and thus, the collected data must be processed in an unconventional manner.

Unlike conventional marine data processing, unconventional processing has two characteristics. First, the spatial distribution of detectors in the acquisition system is very irregular; second, it is necessary to use all the data collected in different ways. The primary difficulty lies in the fact that the coverage angle range of the data is likely to exceed the conventional reflection angle range, and the full offset assumption of the conventional overlay is not satisfied; moreover, the imaging resolution is much higher than the conventional processing range, and thus, the sampling rate needs to be reconsidered. Therefore, it is necessary to carefully design and develop methods to perform unconventional modeling, imaging and attribute extraction that mimic a stereoscopic detection

system to make full use of acquired wide-angle, wide-band, high-signal-to-noise ratio seismic data. In general, no research has been performed on the joint imaging of stereoscopic acquisition data either at home or abroad; rather, most domestic and foreign experts are focused on different migration imaging and processing methods for data using a single system. Therefore, joint imaging research for stereoscopic detection will constitute an effective driving force on domestic researchers investigating seismic imaging.

Research should also be performed on the anisotropy of hydrate reservoirs based on stereoscopic data. Stereoscopic detection networks provide characteristically wide-angle, wide-band, high-signal-to-noise ratio, multiscale data. Hence, performing research on the heterogeneity of hydrate formations and reservoirs based on the characteristics of stereoscopic observation data could have great guiding significance for the continued development and utilization of hydrate resources.

Based on the joint observation of OBS multi-component data and streamer data, high-precision imaging of large-scale stratigraphic structures can be realized, which provides some evidence for the formation and evolution process of the South China Seawater reservoir and gas source conditions. The sensitive factor of hydrate reservoir is the product of the combination of rock physical properties and acoustic characteristics of the formation medium, and it is the most intuitive expression of the physical properties of the target layer. Further study on the sensitive attribute factors of reservoirs and structures other than hydrates can be done, for example, based on the formation of lithology division and geological age division by velocity structure analysis, establishing the relationship equation between geological time and stratum physical parameters and elastic parameters. It can provide new ideas for geological interpretation and improve the accuracy of geological interpretation.

6 Conclusion

(1) The natural gas hydrate storage characteristics in the Shenhu Sea area are perfect. Since the Paleogene (23.8 Ma), the Enping Formation and Wenchang Formation at great

depth in the study area have exhibited a large number of hydrocarbon generation stages. During the Dongsha movement, the fault structure was active; therefore, a large amount of pyrite dissolved within fluids was transported upwards from deeper strata to shallower strata through an active fault (a regional large-scale fault). When free gas was transported to the Pliocene and during the Quaternary period, it became connected to Pliocene and Quaternary deepwater fan faults and slip faults, and the free gas diffused laterally through horizontal faults continuously. Since the Quaternary sedimentary layers are dense, the free gas was transported upwards until it encountered a trap environment, where it continued to accumulate before finally becoming a hydrate deposit.

(2) OBS and VC data are important components of stereoscopic detection system data for hydrate resources. OBS and VC single-node codetection wave point data volumes are used to apply horizontal and vertical constraints on velocity models obtained by streamer data based on a ray-based traveltimes inversion method to further correct the initial model and improve the imaging quality of the streamer data.

(3) Among the many hydrate-sensitive parameters, the sensitivity of $\lambda\rho$ to hydrate is basically the same as that of V_p , and even the sensitivity of $\lambda\rho$ is greater than those of V_p and $\lambda\mu$. When the hydrate saturation is less than 0.35, $\mu\rho$, V_s and σ are less sensitive to hydrate, while σ is more ambiguous to the spatial distribution of hydrate, and its sensitivity to free gas is greater than that to hydrate. At the same time, the greater the number of sensitive parameters in the constraints applied, the higher the accuracies of the hydrate reservoir description and saturation estimation. Finally, the bulk modulus of the hydrate reservoir in the Shenhu Sea area is more sensitive to the saturation level than its shear modulus.

7 Acknowledgements

The study is supported by the Fund of Acoustics Science and Technology Laboratory (KY1050019005, KY1050019006, KY10500180084), National Natural Science Foundation of China (Nos.41304096, 41876053), the Fundamental Research Funds for the Central Universities (HEUCFJ180503), the National Science and Technology Major Project of China (2016ZX05024-001-002), National key research and development plan (2017YFC0307401), Fundamental Research Funds for the Central Universities (201762019).

8 Reference

Asakawa, E., Murakami, F., Sekino, Y., 2012. Vertical Cable Seismic Survey for Hydrothermal Deposit[C] EGU General Assembly Conference. EGU General Assembly Conference Abstracts.

- Asakawa, E., Murakami, F., Tsukahara, H., 2015. Development of vertical cable seismic (VCS) system for seafloor massive sulfide (SMS)[C] Oceans - St. John's. IEEE, 1-7.
- An, Z.F., Zhang, J., Zhang, J.Z., 2018. Geometry Optimization Design of three dimensional marine vertical cable[J]. Journal of jilin University. 48(1): 271-284.
- Bian, A.F., Zhi, H., 2015. Evaluation of Multi-Scale Full Waveform Inversion with Marine Vertical Cable Data[J]. Journal of Earth Science, 26(4): 481-486.
- Dash, R., Spence, G.D., 2011. P-wave and S-wave velocity structure of northern Cascadia margin gas hydrates. Geophy. J. Int. 187 (3): 1363-1377.
- Exley, R.J.K., Westbrook, G.K., Haacke, R.R., 2010. Detection of Seismic anisotropy using ocean bottom seismometers: a case study from northern headwall of Storegga Slide. Geophy J. Int, 183 (1): 188-210.
- Fu, S.Y., Lu, J.A., 2010. The characteristics and origin of gas hydrate in shenhu area, south china sea[J]. Marine Geology Letters. 26(9): 6-10.
- Huang, J.Y., Wu, Z.L., Wang, W.W., 2016. Key Techniques and Experimental Study of Vertical Cable Seismic System for Gas Hydrate[J]. ADVANCES IN NEW AND RENEWABLE ENERGY. 4(3): 219-224.
- Hao, Z.G., Fei H.C., Hao, Q.Q., 2017. China Has Successfully Conducted its First Pilot Production of Natural Gas Hydrates[J]. Acta Geologica Sinica - English Edition, 91(3):1133-1134.
- Herri, J.M., Pic, J.S., Gruy, F., 1999. Methane hydrate crystal-lization mechanism from in-situ particle sizing[J]. AIChE Journal, 45(3): 590-602.
- Kvenvolden, K.A., 1995. A review of the geochemistry of methane in natural gas hydrate[J]. Organic Geochemistry, 23(11-12): 997-1008.
- Kumar, D., Sen, M.K., Bangs, N.L., 2006. Gas Hydrate concentration and characteristics within Hydrate Ridge inferred from multi-component seismic data. J. Geophysical Research, 112, B12306.
- Li, J.F., Ye, J.L., Xu, W.Q., 2018. The first offshore natural gas hydrate production test in South China Sea[J]. China Geology, 1: 5-16.
- Liao, J., Gong, J.M., Lü, W.J., 2016. Simulation of the Accumulation Process of Biogenic Gas Hydrates in the Shenhu Area of Northern South China Sea[J]. Acta Geologica Sinica(English Edition), (06):357-358.
- Mienert, J., Bünz, S., Guidard, S., 2005. Ocean bottom seismometer investigations in the Ormen Lange area offshore mid-Norway provide evidence for shallow gas layers in subsurface sediments[J]. Marine & Petroleum Geology, 22(1-2): 287-297.
- Naehr, T.H., Rodriguez, N.M., Bohrmann, G., 2000. Methane-derived authigenic carbonates associated with gas hydrate decomposition and fluid venting above the Blake Ridge Diapir[J]. Proceedings of the Ocean Drilling Program Scientific Results, 164: 285-300.
- Peacock, S., Westbrook, G.K., Bais, G., 2010. S-wave velocities and anisotropy in sediments entering the Nankaisubduction zone, offshore Japan. Geophy. J. Int, 180, 743-758.
- Petersen, C.J., Papenberg, C., Klaeschen, D., 2007. Local seismic quantification of gas hydrates and BSR characterization from multi-frequency OBS data at northern Hydrate Ridge[J]. Earth & Planetary Science Letters, 255(3-4): 414-431.
- Pierre, H., Michel, T., Ben, C., 1999. Formation of natural gas hydrates in marine sediments, thermodynamic calculations of stability conditions in porous sediments[J]. Journal of Geophysical Research, 104 (B10): 23005-23022.
- Sha, Z.B., Zhang, M., Zhang, G.X., 2015. Using 4C

- OBS to reveal the distribution and velocity attributes of gas hydrates at the northern continental slope of South China Sea[J]. *Applied geophysics*, 12(4): 555–563.
- Satyavani, N., Kalachand. Sain., 2015. Seismic Insights into Bottom Simulating Reflection (BSR) in the Krishna-Godavari Basin, Eastern Margin of India[J]. *Marine Georesources&Geotechnology*, 33(3): 191–201.
- Satyavani, N., Sain, K., Jyothi, V., 2014. Gas hydrate occurrences in the Andaman offshore, India-Seismic inferences. *Jour. Indian Geophysics. Union*, 18 (4): 440–447.
- Singh, P.K., Sain, K., 2012. 2–D velocity structure in Kerala-Konkan basin using travelttime inversion of seismic data[J]. *Journal of the Geological Society of India*, 79(1): 53–60.
- Trotskyuk, V.Y., Nemirovskaya, N.A., 1985. Hydrocarbon gas hydrate formation beneath the sea floor[J]. *International Geology Review*, 27(11): 1325–1328.
- Ward, Huang, B.M., 1998. The seismic value of vertical cable[J]. *Oil and gas reservoir evaluation and development*. (5): 81–85.
- Wang, X., Qian, R., Xia, C., 2014. PS wave processing and S-wave velocity inversion of OBS data from Northern South China Sea. *J. Appl. Geophys*, 100, 58–65.
- Westbrook, G.K., Chand, S., Rossi, G., 2008. Estimation of gas hydrate concentration from multi-component seismic data at sites on the continental margins of NW Svalbard and the Storegga region of Norway[J]. *Marine & Petroleum Geology*, 25(8): 744–758.
- Wu, N.Y., Liu, C.L., Hao, X.L., 2018. Experimental simulations and methods for natural gas hydrate analysis in China[J]. *China Geology*. 1: 61–71.
- Wu, Z.L., Ma D.T., Sha Z.B., 2011. Study on layout design methods of ocean bpttom seismic[J]. *Journal of xian University of science and technology*. 31(2): 194–197.
- Wan, K.Y., Cao, J.G., Xia, S.H., 2016. Characteristics of secondary Pg phases from OBS wide-angle seismic survey and their role in crustal imaging[J]. *Chinese Journal of geophysics*. 59(8): 2818–2832.
- Waseda, A., 1998. Organic carbon content, bacterial methanogenesis, and accumulation processes of gas hydrates in marine sediments[J]. *Geochemical Journal*, 32(3): 143–157.
- Xia, C.L., Liu, X.W., Xia, M.L., 2008. Submarine gas hydrate detecting by application of OBS[J]. *Progress in Exploration Geophysics*, 31(4): 259–264.
- Ye, J.L., Xu, W.Q., Qiu, H.J., 2018. Preliminary results of environmental monitoring of the natural gas hydrate production[J]. *China Geology*. 2: 202–209.
- Zhang, M., 2016. Geochemical Characteristics of C5–C7 Light Hydrocarbons in Gas Hydrates from the Permafrost Region of Qilian Mountains[J]. *Acta Geologica Sinica (English Edition)*, 90(6):2283-2284.
- Zhu, C.Q., Jia, Y.G., 2017. In-situ Observations of Engineering Geological Environment during Hydrate Production Tests in Deepwater[J]. *Acta Geologica Sinica(English Edition)*, (S1): 207–208.
- Zhang, G.X., Xu, H.N., Liu, X.W., 2014. The acoustic velocity characteristics of sediment with gas hydrate revealed by integrated exploration of 3D seismic and OBS data in Shenhu area[J]. *Chinese Journal of Geophysics*. 57(4): 1169–1176.
- Zhao, W.N., Zhang, X.H., Meng, X.J., 2017. Analysis of converted shear-waves based on OBS data in the South Yellow Sea and its geological implications. *Chinese journal of geophysics*. 60(4): 1479–1490.
- Xia, S.H., Cao, J.H., Wan, K.Y., Fan, C.Y., 2016. Role of the Wide-angle OBS Seismic Exploration in the Research of Marine Sedimentary Basin. *Advances in earth science*, 31(11): 1111–1124.
- Qiu, X.L., Zhao, M.H., Ao, W., 2011. OBS survey and crustal structure of the Southwest Sub-basin and Nansha Block, South China Sea[J]. *Chinese Journal of Geophysics*, 54(12): 3117–3128.
- Su, M., Yang, R., Wu, N.Y., Wang, H.B., Liang, J.Q., Sha, Z.B., 2014. Structural Characteristics in the Shenhu Area, Northern Continental Slope of South China Sea and Their Influence on Gas Hydrate. *Acta geological sinica*, 88(3): 318–326.
- Cong, X.R., Yu, X.H., Su, M., Sha, Z.B., 2013. Tectonic subsidence characteristics on the northern continental Margin of the South China Sea since Late Miocene. *Journal of tropical oceanography*, 32(6): 42–49.
- Yu, X.H., Zhang, Z.J., Su, X., Chen, F., Li, Y., 2004. Primary discussion on accumulation conditions for sedimentation of gas hydrate and its distribution in south china sea. *Earth Science Frontiers*, 11(1): 311–315.

About the first author

LIU Xueqin, female, born in 1989 in Laiwu City, Shandong Province; doctor; graduated from Ocean University of China; Lecturer, Harbin Engineering University. She is now interested in the study on Marine science and Hydroacoustic engineering. Email: 1226535203@qq.com; phone: 15588670510.



About the corresponding author

QIN Zhiliang, male, born in 1983 in Taizhou City, Jiangsu Province; doctor; graduated China University of Petroleum; PhD Tutor, Harbin Engineering University. He is now interested in the study on Marine science and Hydroacoustic engineering. Email: qin_zhiliang@126.com; phone:15301080807.